JOURNAL OF PROPULSION AND POWER
Vol. 11, No. 3, May–June 1995

Gravity Effects on the Dynamics of Evaporating Droplets in a Heated Jet

T. W. Park* and S. K. Aggarwal†
University of Illinois at Chicago, Chicago, Illinois 60607
and
V. R. Katta‡
System Research Laboratory, Inc., Dayton, Ohio 45440

Dispersion and vaporization behavior of liquid fuel droplets in a heated axisymmetric jet is studied using detailed flow visualization based on numerical simulations. Results show that the gravity has a strong effect on the dynamics of jet shear layer and droplets. The presence of gravity introduces the buoyancy-induced hydrodynamic instability, causing the large vortical structures to appear without any external perturbation. The droplet dispersion and vaporization behavior is influenced by both the vortex structures and the gravity. Three regimes, distinguished by the Stokes number *St* and the ratio of droplet terminal velocity to characteristic gas velocity *Vr*, are identified to characterize the effects of vortex structures and gravity on droplet dispersion. At low *St* and *Vr*, the droplets behave like gas particles. In the second regime, $0.1 < St < 0.64$ and $0.04 < Vr < 0.3$, due to the centrifugal action of the vortex structures the droplets are dispersed more than the gas particles. At the lower end of the third regime, the droplet motion is affected by both the vortex structures and the gravity, whereas at the higher end it is affected more by gravity. The effect of vaporization is to shift the Stokes number range for the three regimes.

Nomenclature

B = Spalding transfer number
C_D = droplet drag coefficient
C_p = specific heat
D = vapor/air binary diffusion coefficient
d_k = droplet diameter
g = acceleration of gravity
H = heat transferred from gas phase to droplet per unit mass of fuel vaporized
$\bar{H}$ = H/L
h = heat transfer coefficient
L = latent heat of vaporization
Le = Lewis number, $\lambda/(\rho D C_p)$
M = molecular weight
$\dot{m}_k$ = droplet vaporization rate
$\dot{m}''_k$ = droplet vaporization flux rate, $\dot{m}_k/(\pi d_k^2)$
$\bar{m}_k$ = normalized droplet vaporization rate, $\dot{m}_k/(2\pi\rho D d_k)$
Nu = Nusselt number
P = pressure
Pe = Peclet number, $RePr$
Pr = Prandtl number
R = universal gas constant
Re = Reynolds number
r = radial distance for gas-phase
Sc = Schmidt number
Sh = Sherwood number
St = Stokes number, t_k/t_f
T = temperature
T_B = boiling temperature
T_0 = initial droplet temperature
t = time
t_f = characteristic flow time
t_k = droplet aerodynamic response time, $\rho_k d_k^2/(18\mu_g)$
u = axial velocity
V_t = droplet terminal velocity, $\rho_k d_k^2 g/(18\mu_g)$
v = radial velocity
x = axial location of droplet
Y = mass fraction
y = radial location of droplet
z = axial distance
α = thermal diffusivity
λ = thermal conductivity
μ = dynamic viscosity
ρ = density

Subscripts
F = fuel vapor
g = gas-phase
i = ith species
k = droplet characteristic or group
l = liquid-phase
s = surface
∞ = ambient condition

Received May 27, 1994; revision received Sept. 2, 1994; accepted for publication Sept. 16, 1994.

*Graduate Student, Department of Mechanical Engineering. Student Member AIAA.
†Associate Professor, Department of Mechanical Engineering. Associate Fellow AIAA.
‡Senior Engineer. Member AIAA.

Introduction

GRAVITY influences combustion phenomena in many significant ways. Combustion systems where gravity plays a key role include burning droplets, jet diffusion flames, freely propagating premixed flames, candle flames, flames over solid and liquid pools, and other heterogeneous flames.[1] Since the pioneering work of Burke and Schumann[2] and Hottel and Hawthorne,[3] the gaseous diffusion flames, because of their practical and scientific importance, have been extensively studied over many decades. More recently, opportunities provided by the microgravity (μg) environment at ground-based and space facilities have motivated additional research in this area, focusing on the effects of gravity on the diffusion flames.[4–9] It has been found[4–9] that the reduction of gravity introduces drastic changes in both the steady-state and the dynamic characteristics of these flames. Under μg conditions,

the diffusion becomes a more dominant transport mechanism and the residence time is increased. Consequently, the μg diffusion flames are much taller, wider, sootier, and more radiating compared to the corresponding normal gravity ($1g$) flames. The μg and $1g$ flames also differ in structural details and their dependence on pressure, oxygen concentration, and Reynolds number. In addition, the $1g$ flames are subjected to the buoyancy-induced hydrodynamic instability, which is responsible for the presence of large vortical structures outside of the flame.[7-9] These low-frequency, slowly moving outer structures interact strongly with the flame surface, creating a wrinkled flame, and are responsible for the flame flicker. In μg conditions, these structures are not present.

The transitional behavior of diffusion flames also exhibit fundamental differences in $1g$ and μg conditions.[5,6] At $1g$, transition is first observed at the flame tip, and with increasing Reynolds number, instability moves closer to the flame base. At μg, transition is associated with the appearance of intermittent disturbances that form at the base and move downstream. In addition, the buoyancy-generated turbulence aids in transition to turbulent flame at $1g$, whereas the transition occurs over a much longer range of Reynolds number at μg. The blowoff limits are also significantly extended for μg diffusion flames.

While the gaseous diffusion flames under $1g$ and μg conditions have been extensively investigated, the research focusing on the effects of gravity on liquid-fuel spray diffusion flames is rather limited. Additional complications arising from gravity in a spray flame are due to the effect of gravity on droplet motion, causing droplet settling and stratification in droplet concentration, and the dynamic interactions of droplets with outer buoyancy-driven structures. These interactions, which involve the influence of outer structures on the dispersion and vaporization behavior of droplets, and the effect of dispersed phase on the development of buoyancy-driven instability, are expected to play an intrinsic role in the dynamics of spray flames.

In this article, the dynamics and dispersion behavior of *n*-heptane droplets in a heated axisymmetric jet is studied via numerical simulations. The gravity is considered a parameter. The overall objective is to study the fundamental processes of spray diffusion flames in laminar and transitional regimes under the influence of gravity. In this first study, the physical model is simplified by considering a heated jet issuing into a slower cold coflow, so that the complexities due to chemical reactions and the effects of dispersed phase on gas-phase processes can be avoided. The dispersion behavior of nonevaporating and evaporating droplets injected into the jet shear layer, where the fluid dynamics and heat transport processes are dominated by buoyancy-induced vortical structures, is investigated. Results presented focus on the effect of evaporation on the droplet dispersion behavior in the presence of large vortex structures, and the role of gravity in the dispersion process. Several experimental and computational studies[10-18] have been reported in recent years, examining the dispersion behavior of particles or nonevaporating droplets in the presence of shear-induced vortex structures. These studies indicate that the dynamics of particles in the near shear-layer region is controlled by the large structures, which enhance the dispersion of intermediate size particles. The effect of vortex structures on particle dispersion is characterized by *St*, defined as the ratio of the particle response time to the characteristic flow time. The cited studies, however, do not consider the effect of evaporation on the dispersion behavior.

Physical Model

Figure 1 shows the physical system simulated in the present study. The heated air jet at a velocity of 1.0 m/s and temperature of 1200 K issuing into a coflow at velocity of 0.2 m/s and temperature of 294 K is considered. The jet diameter is 2.54 cm, and the computational domain in the radial direction is 15 cm. For the heated jet at $1g$, the buoyancy-induced vortex structures are observed in the jet shear layer. The dynamics of these structures is simulated by solving the time-dependent, axisymmetric gas-phase equations. The *n*-heptane droplets of different diameters are then injected into the jet shear layer from the specified radial locations, and their dispersion and vaporization behavior is investigated by solving the appropriate droplet equations.

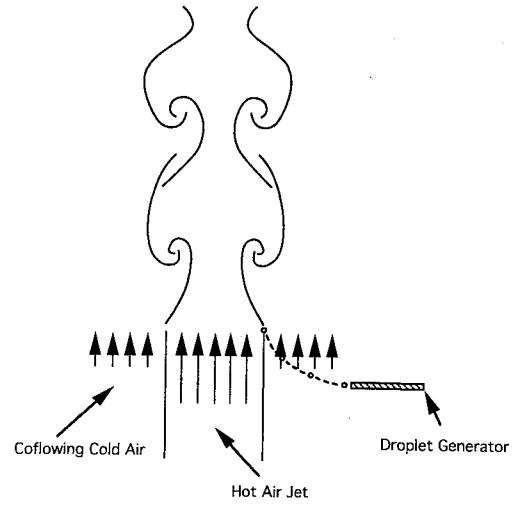

Fig. 1 Schematic of a buoyant hot air jet in a coflowing cold airstream at $1g$.

Gas-Phase Equations

The time-dependent governing equations written in cylindrical (z, r) coordinate system for an axisymmetric heated jet are

$$\frac{\partial(\rho\Phi)}{\partial t} + \frac{\partial(\rho u\Phi)}{\partial z} + \frac{\partial(\rho v\Phi)}{\partial r} = \frac{\partial}{\partial z}\left(\Gamma^{\Phi}\frac{\partial\Phi}{\partial r}\right) + \frac{\partial}{\partial r}\left(\Gamma^{\Phi}\frac{\partial\Phi}{\partial z}\right) - \frac{\rho v\Phi}{r} + \frac{\Gamma^{\Phi}}{r}\frac{\partial\Phi}{\partial r} + S_g^{\Phi} \tag{1}$$

The general form of Eq. (1) represents the continuity, momentum, or energy equation, depending on the variable used for Φ. Table 1 gives the transport coefficients Γ^{Φ} and the source terms S_g^{Φ} that appear in the governing equations. In this table, μ, λ, and C_p are, respectively, the viscosity, thermal conductivity, and specific heat of air. They are considered functions of temperature.

Liquid-Phase Equations

The Lagrangian approach is employed to compute the properties of each droplet as it travels in a heated jet shear flow. The equations governing the variation of position, velocity, and size for a given droplet k along its trajectory are

$$\frac{dx_k}{dt} = u_k \tag{2}$$

$$\frac{dy_k}{dt} = v_k \tag{3}$$

$$\frac{du_k}{dt} = \frac{3C_D\rho_g}{4d_k\rho_k}|u_g - u_k|(u_g - u_k) + \left(\frac{\rho_g}{\rho_k} - 1\right)g \tag{4}$$

$$\frac{dv_k}{dt} = \frac{3C_D\rho_g}{4d_k\rho_k}|v_g - v_k|(v_g - v_k) \tag{5}$$

$$\frac{dd_k}{dt} = -\frac{2\dot{m}_k''}{\rho_k} \tag{6}$$

Table 1 Transport coefficients and source terms appearing in governing equations

Equations	Φ	Γ^Φ	S_g^Φ
Continuity	1	0	0
Axial momentum	u	μ	$-\frac{\partial p}{\partial z} + (\rho_0 - \rho)g + \frac{\partial}{\partial z}\left(\mu\frac{\partial u}{\partial z}\right) + \frac{\partial}{\partial r}\left(\mu\frac{\partial v}{\partial z}\right) + \frac{\mu}{r}\frac{\partial v}{\partial z} - \frac{2}{3}\left[\frac{\partial}{\partial z}\left(\mu\frac{\partial u}{\partial z}\right) + \frac{\partial}{\partial z}\left(\mu\frac{\partial v}{\partial r}\right) + \frac{\partial}{\partial z}\left(\mu\frac{v}{r}\right)\right]$
Radial momentum	v	μ	$-\frac{\partial p}{\partial r} + \frac{\partial}{\partial z}\left(\mu\frac{\partial u}{\partial r}\right) + \frac{\partial}{\partial r}\left(\mu\frac{\partial v}{\partial r}\right) + \frac{\mu}{r}\frac{\partial v}{\partial r} - 2\mu\frac{v}{r^2} - \frac{2}{3}\left[\frac{\partial}{\partial r}\left(\mu\frac{\partial u}{\partial z}\right) + \frac{\partial}{\partial r}\left(\mu\frac{\partial v}{\partial r}\right) + \frac{\partial}{\partial r}\left(\mu\frac{v}{r}\right)\right]$
Energy	T	λ/C_p	0

where

$$C_D = \frac{24}{Re_k}\left(1 + \frac{Re_k^{2/3}}{6}\right) \tag{7}$$

$$Re_k = \frac{\rho_g[(u_g - u_k)^2 + (v_g - v_k)^2]^{1/2} d_k}{\bar{\mu}_g} \tag{8}$$

The following expressions[19] are used for heat and mass transfer rates to the drop:

$$\frac{h d_k}{\lambda} = \frac{2(N_P/Le)\,\ln(1 + B)}{(1 + B)^{1/Le} - 1} \tag{9}$$

$$\frac{\dot{m}_k'' d_k}{\rho D} = 2N_S\,\ln(1 + B) \tag{10}$$

and B is given by

$$B = (Y_{Fs} - Y_{F\infty})/(1 - Y_{Fs}) \tag{11}$$

N_p and N_s are the corrective factors to consider the convective effect on heat and mass transfer, and are calculated using semi-empirical relations[19]:

$$N_P \text{ or } N_S = 1 + \frac{0.278 Re_k^{1/2}(Pr \text{ or } Sc)^{1/3}}{[1 + 1.232/(Re_k(Pr \text{ or } Sc)^{4/3}]^{1/2}} \tag{12}$$

In order to complete the solution, the drop surface temperature and the fuel mass fraction at the drop surface must be known. The two equations required to solve for these quantities are provided by the fuel vapor pressure relationship and the energy equation in the liquid. The vapor pressure relationship has the form

$$Y_{Fs} = f(T_s, P, Y_{is}) \tag{13}$$

The transient heat transport within the droplet is represented by the unsteady heat diffusion equation in a spherically symmetric geometry. The solution of this equation involves a moving boundary-value problem as the droplet is evaporating. This problem can be reformulated by using a transformation to make the boundary stationary. The transformed governing equation[20] is

$$\frac{\partial \bar{T}_l}{\partial \bar{t}} = \frac{1}{\bar{r}^2}\frac{\partial}{\partial \bar{r}}\left(\bar{r}^2\frac{\partial \bar{T}_l}{\partial \bar{r}}\right) - \frac{\bar{r}\dot{m}_k\lambda}{LeC_p\rho_l\alpha_l}\left(\frac{\partial \bar{T}_l}{\partial \bar{r}}\right) \tag{14}$$

with the initial and boundary conditions as

$$\bar{T}_l = 0 \quad \text{at} \quad \bar{t} = 0 \tag{15}$$

$$\frac{\partial \bar{T}_l}{\partial \bar{r}} = 0 \quad \text{at} \quad \bar{r} = 0 \tag{16}$$

$$\frac{\partial \bar{T}_l}{\partial \bar{r}} = \frac{\dot{m}_k(\bar{H} - 1)L\lambda}{LeC_p\lambda_l(T_B - T_0)} \quad \text{at} \quad \bar{r} = 1 \tag{17}$$

where $\bar{T}_l(\bar{r}, \bar{t})$ and $\bar{r}$ are, respectively, the normalized liquid temperature and radial location inside the droplet, and $\bar{t}$ is the normalized time variable. These are given by

$$\bar{T}_l = (T_l - T_0)/(T_B - T_0) \tag{18}$$

$$\bar{r} = 2r/d_k \tag{19}$$

$$\bar{t} = \alpha_l\int_0^t \frac{4}{d_k^2}\,dt \tag{20}$$

The vapor pressure relationship and other properties used for the liquid and gas phases are summarized in the Appendix. The droplet model includes the effects of variable thermophysical properties and nonunity Lewis number in the gas film outside the droplet. The thermophysical properties are calculated at an average reference state defined as

$$\Phi_{\text{avg}} = \alpha\Phi_{gs} + (1 - \alpha)\Phi_g \tag{21}$$

where Φ is a generic quantity representing either mass fraction or temperature, and α is selected to be 0.7. The subscripts gs and g represent the gas-phase property at the droplet surface and outside the gas film, respectively.

It should be noted that in the present vaporization model, the effect of transient heating is incorporated by using the conduction-limit model.[20] This model is deemed satisfactory in the present study, since the maximum droplet Reynolds number during droplet lifetime is less than 10, and, therefore, the effect of internal circulation is expected to be negligible. For the same reason, the effect of gas-phase convection on the heat and mass transport is represented by semi-empirical correlations, Eq. (12).

Numerical Model

An implicit algorithm is employed to solve the unsteady gas-phase equations. The finite difference forms of the momentum equations are obtained using an implicit QUICKEST scheme.[21] The governing equations are integrated on a nonuniform staggered-grid system. An iterative alternative direction implicit (ADI) technique is used for solving the resulting sets of algebraic equations. At every time step, the pressure field is calculated by solving the pressure Poisson equations simultaneously and utilizing the lower and upper diagonal (LU) matrix decomposition technique.

Figure 2 shows the grid system and the computational domain used in the present study. Grid lines are clustered near the shear layer to resolve the steep gradients of the dependent variables. Boundaries of the computational domain are shifted sufficiently to minimize the propagation of disturbances into region of interest. The flow variables at the outflow boundary are obtained using an extrapolation procedure with weighted zero and first-order terms. The main criterion used in selecting the weighting functions is that the vortices crossing this outflow boundary should leave smoothly without being distorted.

The liquid-phase equations are advanced in time by a second-order accurate Runge–Kutta method. Since the gas-phase

solution employs an implicit procedure, the temporal step size used for integrating the liquid-phase equations is usually smaller than that for gas-phase equations. An automatic procedure is implemented in order to select an optimum liquid-phase time step. The procedure involves calculating the characteristic thermal response time, velocity response time, and vaporization time for each droplet group, and then selecting the temporal step size as a fraction (two-hundredth) of the smallest of these time scales. A detailed examination of the various time scales, based on numerical experiments, revealed that the temporal step size is determined by either the thermal response time or the velocity response time of a given droplet group. The number of subcycles for advancing the liquid-phase solution for each gas-phase cycle typically varies from 1 to 30, depending upon the droplet size.

The procedure to advance the two-phase solution over one gas-phase time step Δt_g is as follows. Using the known gas-phase properties, the liquid-phase equations are solved over the specified number of liquid-phase subcycles. A third-order accurate Lagrangian polynomial method is used for interpolating the gas-phase properties from the nonuniform fixed grid to the droplet characteristic location. Figure 3 shows the gas-phase cells surrounding a droplet characteristic. The variable $\Phi_{g,k}$ represents the interpolated value of the gas-phase variable at the k-characteristic location. It should be noted that the interpolation scheme for the gas-phase velocities u and v is based on their respective grid cells because of the use of a staggered grid in gas-phase calculation. It is also important to find the best-fit nine grid points at each characteristic location for better interpolation. The nine grid points shown in Fig. 3 correspond to the characteristic location in the shaded region. The droplet properties are updated after every liquid-phase subcycle. The gas-phase properties are then updated by solving Eq. (1), as desribed earlier.

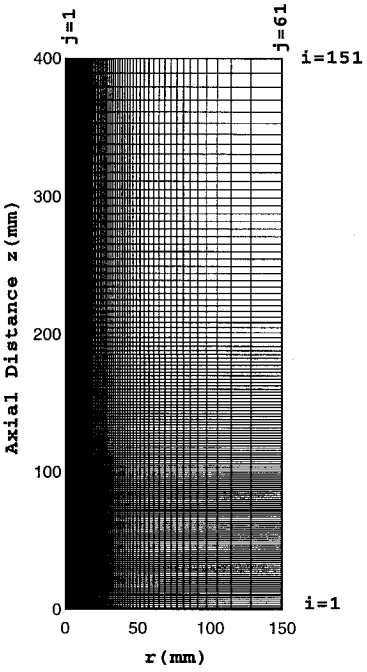

Fig. 2 Typical grid system used for simulations.

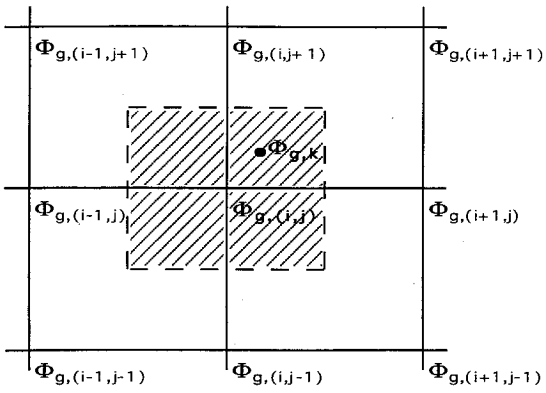

Fig. 3 Best-fit grid cells for the interpolation.

Results and Discussion

For the base case, a jet at a velocity of 1.0 m/s and temperature of 1200 K issuing into a coflow at a velocity of 0.2 m/s and temperature of 294 K is considered. The computational domain is 15 cm in the radial direction and 40 cm in the axial direction. The jet diameter is 2.54 cm. A nonuniform grid system with 151 × 61 grid points, with a large number of grid points clustered in the shear layer, is utilized. The minimum grid spacing is about 0.079 cm, and the Courant, Friedrichs, and Lewy (CFL) number is 0.2. Several diagnostic runs were made to assure that the gas-phase simulations are reasonably independent of the grid size and CFL number. Results from one of these runs, indicating the grid-independence of the gas-phase solution, are given in Fig. 4, which shows the instantaneous iso-temperature contours for two grid densities for the heated jet at 1g. The effect of CFL number on the gas-phase solution was also evaluated, and the CFL number of 0.2 was found to be in the range where the solution is insensitive to the temporal step size Δt_g. The temporal step size for droplet calculation Δt_p was also taken in the range where the droplet results are independent of Δt_p, as described earlier.

Dynamics of Cold and Heated Jets

The stability characteristics of cold and heated jets under 0 and 1g conditions are examined first without injecting droplets into the jet shear layer. Based on the jet velocity of 1.0 m/s and the diameter of 2.54 cm, the cold and heated jets represent flows with Reynolds number of 1.546×10^3 and 1.50×10^2, respectively. The latter is calculated using the density and viscosity of air at 1200 K. Due to the velocity gradient, the jet shear layer exhibits Kelvin-Helmholtz-type instability, which is characterized by the formation of large toroidal vortices. However, to simulate these vortices a low-amplitude perturbation, either external or inherent in the calculations, is required. Numerical experiments were per-

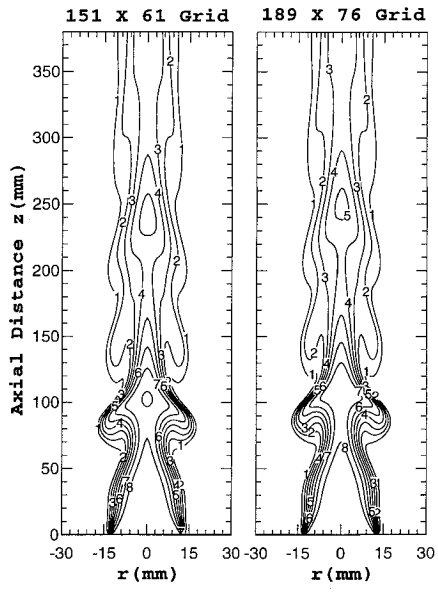

Fig. 4 Comparison of temperature contours for the heated jet with two grid densities.

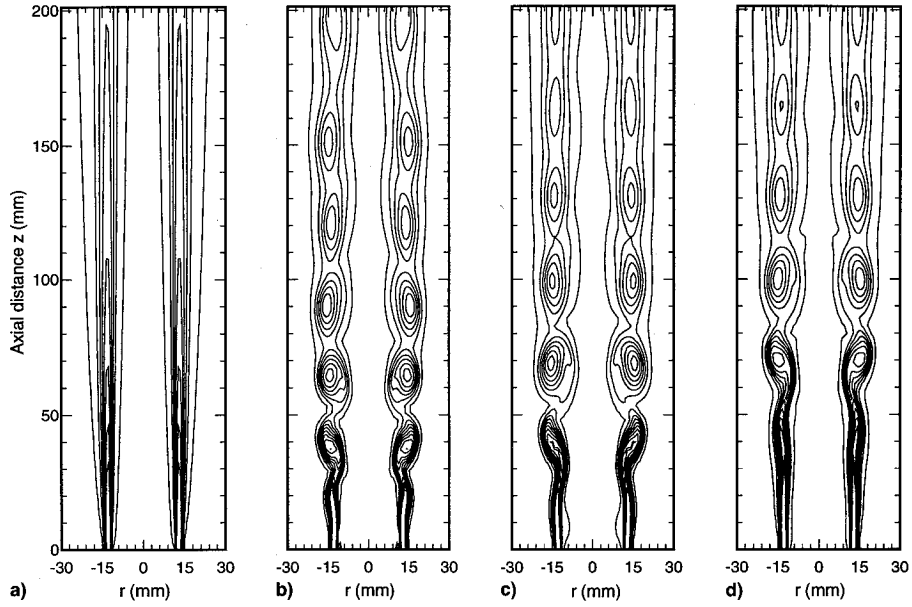

Fig. 5 Iso-vorticity contours for the cold jet for four different cases: a) without external forcing, b) white-noise forcing, c) forcing the central high-speed jet at a frequency of 20 Hz, and d) forcing the low-speed annulus flow at a frequency of 20 Hz. Jet Reynolds number is 1.546×10^3.

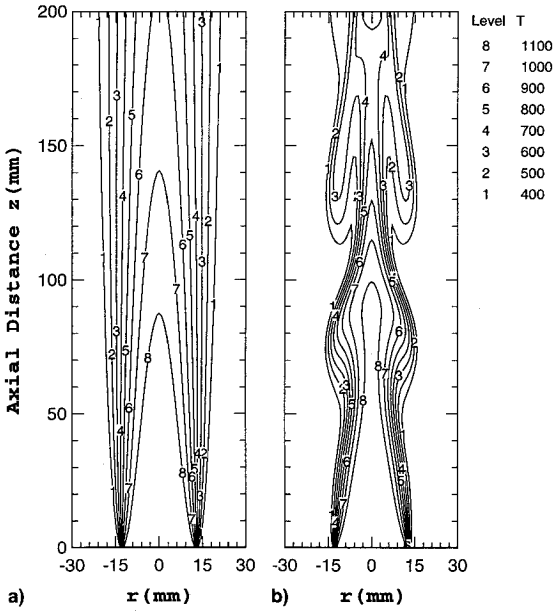

Fig. 6 Iso-temperature contours for the hot jet at a) 0 and b) 1*g*.

formed on these jets for triggering the shear-layer instability and the results are summarized in Figs. 5 and 6.

To determine whether the noise inherent in the calculations is sufficient or not for the development of the shear-layer instabilities, both the cold and heated jets are simulated without introducing any external perturbation. Cold-jet calculations performed with different grid systems and time steps have converged to a steady-state solution that is given in Fig. 5a. The iso-vorticity contours of this figure show that the shear layer is laminar without having flow instabilities. These calculations suggest that the noise in the present simulations is not sufficient for the manifestation and growth of the shear-layer instabilities. Therefore, as an alternative, attempts were made to make the calculated jet shear layer unsteady by providing it with external perturbations.

The following types of external perturbations are considered in the present study: 1) computer-generated white noise superimposed on the convective flow at all the grid points within a circular region of two-grid radius and centered in the jet shear layer at $z = 8$ mm, 2) forcing the entire central high-speed jet to oscillate at a frequency of 20 Hz, and 3) forcing the low-speed annulus flow to oscillate at 20 Hz. Instantaneous vorticity fields resulting from the calculations using the above three types of perturbations are depicted in Figs. 5b–5d, respectively. The magnitude of forcing (velocity fluctuation) for different perturbation modes was fixed at 3% of the local axial velocity. Forcing frequency (20 Hz) used for the latter two modes was equal to the peak-amplification frequency noted from the calculations made with white-noise perturbations (obtained from the fast Fourier transformation of the time data). The iso-vorticity contours of Figs. 5b–5d indicate that all the three types of external perturbation are magnified similarly and resulted in toroidal vortices of same size. Due to the lower-magnitude velocity fluctuations used in the last case (3% of the annulus air velocity of 0.2 m/s) the instability is somewhat weaker (Fig. 5b) in the region $z < 80$ mm compared to that seen for the other two cases (Fig. 5c and 5d).

It is clearly evident from Fig. 5 that the shear layer of the cold jet ($Re = 1.546 \times 10^3$) becomes unsteady only in the presence of external perturbations, and the flow structure seems to be insensitive to the type of perturbation used. For the corresponding heated jet case (jet velocities the same as those of the cold-flow case) the shear layer might be expected to be stable as the effective Reynolds number based on air density and viscosity at 1200 K is reduced by a factor of about 10. Because of the presence of density variation in the heated-jet case, simulations are made by 1) neglecting the gravitational force and 2) assuming that gravity acts in a direction opposite to that of the jet flow, which represents the vertically mounted jets. Computed jets for both the cases are shown in Fig. 6 using iso-temperature contours.

Calculations made by neglecting gravitational force yielded a solution that has no vortical structures in the shear layer (Fig. 6a). Kelvin-Helmholtz instabilities did not develop even when the shear layer was excited using the previously described perturbation methods. However, when the gravity term was introduced in the axial momentum equation, large-scale vortex structures appeared due to the buoyancy-induced instability of the heated-jet shear layer (Fig. 6b). It is important to note that these structures are produced without using any external forcing, and their dynamics are found to be unaltered by the superimposition of the three different external perturbations discussed earlier. This is in contrast to the dynamics of shear-induced vortex structures. The buoyant

acceleration of hot gases at 1*g* helps the formation of large vortex structures, while at 0*g*, due to the low Reynolds number, the jet shear layer exhibits a behavior typical of a laminar flow. The temporal evolution of buoyancy-induced vortices for the 1*g* case is shown in Fig. 7. Computed temperature data along the radial direction at two axial locations are recorded over a period of 250 ms, and the evolution is shown in the form of iso-temperature contours. It can be seen that the vortex structures are highly coherent and periodic. The frequency of oscillation is 15.8 Hz. Even though the frequencies of the Kelvin-Helmholz instability of the cold jet and the buoyancy-induced instability of the heated jet are not much different (20 and 15.8 Hz, respectively), the sizes of the vortical structures in these two cases (Figs. 5b and 6b) are significantly different. The number of vortical structures present within an axial distance of 200 mm in the cold and heated jets are about 6 and 2, respectively. Based on the average vortex size and the crossing frequency, the average convective velocities for the cold and heated jets must be approximately 0.6 and 1.5 m/s, respectively. The higher convective velocity in the case of heated jet is the result of buoyancy.

Effect of Gravity on Droplet Motion

The motion and dispersion characteristics of droplets in the dynamically evolving flow of heated jet (Fig. 6b) are studied by injecting droplets of varying size into the shear layer. Figure 8 shows the effect of gravity on the trajectories of evaporating droplets that are injected at the nozzle rim and traverse the unsteady flowfield dominated by large-scale vortical structures. For this case, the gas-phase simulation is started at $t = 0$ and the droplets are injected at $t = 0.954$ s. During the period of $0 < t < 0.954$ s, the initial flow transient is convected out of the computational domain. The trajectories shown in Fig. 8 are computed from $t = 0.954$–2.226 s by solving the gas-phase and the droplet equations simultaneously. For all the cases considered, the initial droplet velocity is assumed to be equal to the jet velocity. For the 0*g* case (Fig. 8b), due to the absence of buoyant vortex structures, the jet flow has little influence on the droplet trajectory. In particular, there is virtually no radial dispersion of droplets, and the initial droplet size does not have much effect on the trajectory. For the corresponding 1*g* case, however, the droplet motion is strongly influenced by the buoyancy-induced vortex structures. In addition, it may also be affected by gravity directly, depending upon the initial droplet size. In fact, we can identify three different droplet-size regimes given in Table 2, that are distinguished by the Stokes number and the ratio of droplet terminal velocity [$V_t = \rho_k d_k^2 g/(18\ \mu g)$] to characteristic gas velocity. Here, the Stokes number is defined by the ratio of t_k to t_f, the latter defined by the time scale of large structures. At low Stokes number (initial diameter $d_0 < 50\ \mu$m), the droplets behave like gas particles, and gravity has no direct influence on their motion as their terminal velocity is small compared to the characteristic gas velocity ($V_{gas} = 1.5$ m/s), the latter being taken as the average convective velocity of the buoyancy-induced structures. In the second regime, the Stokes number in the range $0.1 < St < 0.64$, the droplet terminal velocity is still small relative to V_{gas}. In this regime, due to the centrifugal action of the vortex structures,[10,16,17] the droplets are dispersed more than the gas particles. This will be discussed quantitatively in the next section. The third regime is characterized by intermediate to large values of the Stokes number. At the lower end of this regime, the droplet motion is affected by both the vortex structures and the gravity, whereas at the higher end, it is affected more strongly by gravity. For example, as shown in Fig. 8, the 500-μm evaporating droplets fall back to the inner jet region due to the strong effect of gravity.

Table 2 Stokes numbers and droplet terminal velocities for various droplet diameters

d_k, μm	St	V_t, m/s
25	0.01	0.006
50	0.04	0.025
100	0.16	0.10
150	0.36	0.23
200	0.64	0.40
250	1.00	0.63
300	1.44	0.90
500	4.00	2.52

Characteristic flow time used in the calculation of Stokes numbers is 0.063 s based on a vortex frequency of 15.8 Hz.

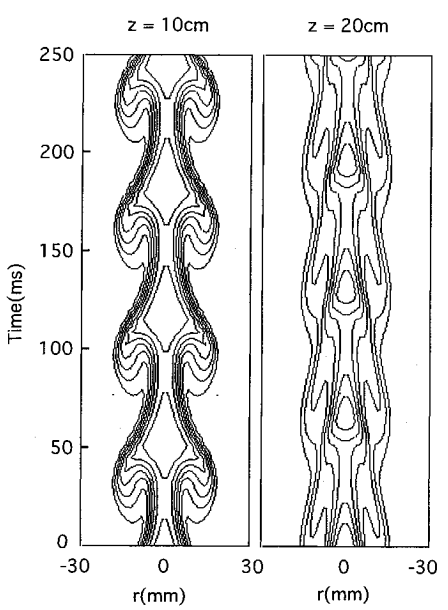

Fig. 7 Temporal evolution of buoyancy-generated vortex structures in terms of iso-temperature contours at two axial locations for the 1*g* case of Fig. 6.

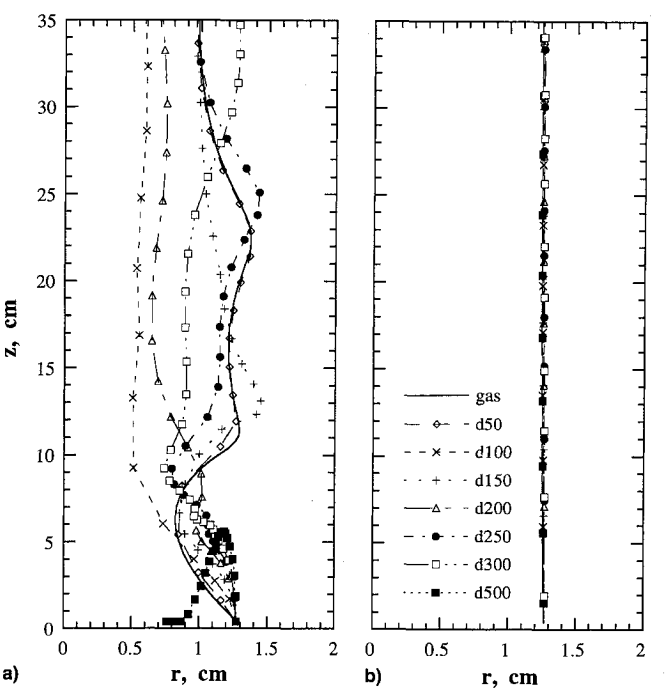

Fig. 8 Trajectories of evaporating droplets injected into the hot jet shear layer under a) 1 and b) 0*g* conditions. Results are shown for a gas particle and droplets of different initial diameters, with *d*50 representing diameter of 50 μm, etc.

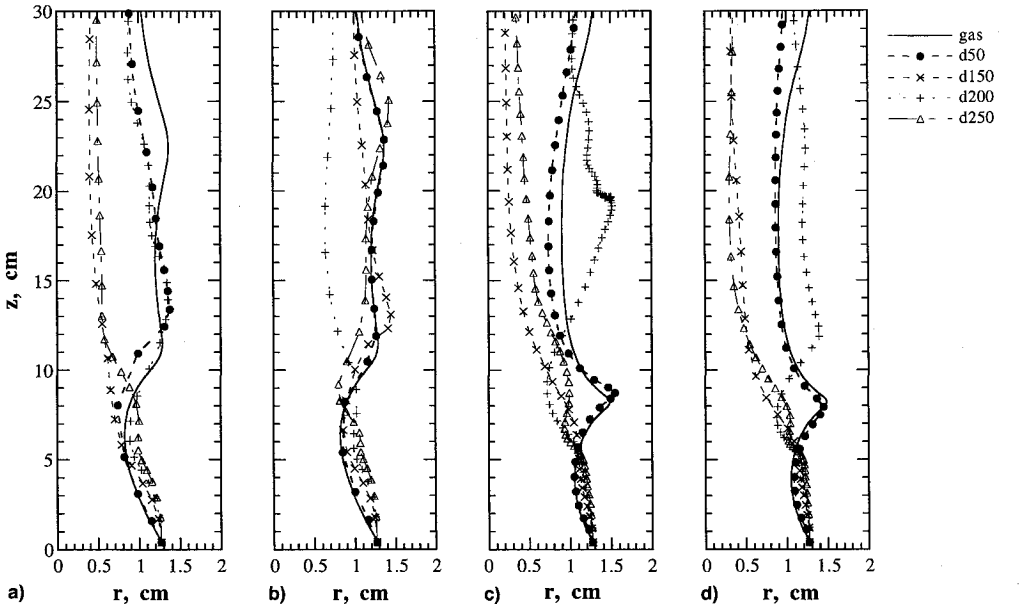

Fig. 9 Trajectories of nonevaporating (a and c) and evaporating (b and d) droplets injected at two different injection times for the 1*g* case. Droplets in a) and b) are injected at $t = 0.954$ s and those in c) and d) at $t = 0.986$ s.

The effect of evaporation on droplet trajectories for the 1*g* case is portrayed in Fig. 9, which shows the trajectories of nonevaporating and evaporating droplets injected at two different times. The difference in the two injection times (t_{dif}) is one-half the time period of the dominant instability frequency, i.e., the droplets in Figs. 9a and 9b are injected at time $t = t_{inj}$, while those in Figs. 9c and 9d are injected at $t = t_{inj} + t_{dif}$. Important observations from this figure are as follows:

1) In the low Stokes number range, the trajectories of evaporating droplets are qualitatively similar to those of nonevaporating droplets, except that the Stokes number decreases along the trajectory for the evaporating case. As a consequence, the evaporating droplets follow the gas motion more closely than the corresponding nonevaporating droplets (see Figs. 9a and 9b).

2) In the intermediate Stokes number range ($0.36 < St < 1.4$), due to the combined effect of vaporization and large structures in a dynamically evolving flowfield, the trajectories of evaporating and nonevaporating droplets are significantly different. For example, compare the trajectories of 200-μm nonevaporating and evaporating droplets in Figs. 9a and 9b, respectively.

3) The droplet trajectory exhibits strong sensitivity to the time (during the dominant instability period) as to when the droplet is introduced into the shear layer. This can be seen by comparing the trajectories of same-size droplets in Figs. 9a and 9c. This sensitivity is important, however, only over the time scale of the dominant frequency. For example, in the dispersion analysis that involves a time scale much longer than the instability time scale, this sensitivity would not be important.

4) The trajectory of a 200-μm droplet is distinctly different from those of 150- and 250-μm droplets. This has some important implication in the size-dependence of the dispersion function discussed in the next section.

Dispersion Behavior

In order to quantify the effects of vortex structures and gravity on droplet dispersion, the dispersion function is defined as

$$D(t, N) = \left(\left\{ \sum_{i=1}^{N} [r_i(t) - r_{io}]^2 \right\} \Big/ N \right)^{1/2} \qquad (22)$$

where N is the total number of droplets in the flowfield at time t, r_i the radial location of droplet i at time t, and r_{io} the radial injection location of the same droplet at nozzle exit. It can be expected that the dispersion function is a strong function of t and droplet diameter d_p. In addition, it may be a function of r_{io}, N, and starting time of injection t_0. In the results presented here, the dispersion function was made statistically independent of N by using a sufficiently large number of droplets in the dispersion calculation, and of t_o by performing calculations over a sufficiently large time t. It is also worth noting that the above dispersion function does not distinguish between the droplets that move away from the jet axis and those that move toward it.

Dispersion behavior of droplets in the heated-jet flow is investigated by continuously injecting single-sized droplets from a given location. Results of the calculations made with a large number of droplet injections are shown in Fig. 10 in the form of simultaneous snapshots (or instantaneous images) of the flow and droplets. Iso-temperature contours are plotted using broken lines and the droplet locations are marked with solid circles. Snapshots for different size droplets are depicted in this figure, whereas in each individual snapshot locations of the evaporating and nonevaporating droplets are plotted on the left and right sides of the symmetric jet, respectively. Color (represents the size) of the droplet changes from red to blue as it evaporates from the initial size (at the instant of injection) to the size of a gas particle, which is taken as 10 μm or one-tenth of the initial size, whichever is smaller. Since the droplets on the right side of the jet represent nonevaporating ones, the color of the droplets remains red. As expected, the snapshot of 50-μm-evaporating droplets shows that these droplets behave like tracer particles and follow the iso-temperature contours. In general, due to the higher momentum, the nonevaporating droplets deviate more from the iso-temperature contours compared to the evaporating ones.

Dispersion of evaporating and nonevaporating droplets in a dynamically evolving flow are quite different. The instantaneous flowfield shown in Fig. 10 has two large-scale vortices that are located approximately at $z = 70$ and 140 mm. The first vortex ($z = 70$ mm) is pulling the smaller size droplets (both the evaporating and nonevaporating ones) radially outward and has little impact on the droplets that are larger than 150 μm. On the other hand, the medium-sized (~150 μm) nonevaporating and smaller evaporating droplets are impacted more by the second vortex ($z = 140$ mm). It may also

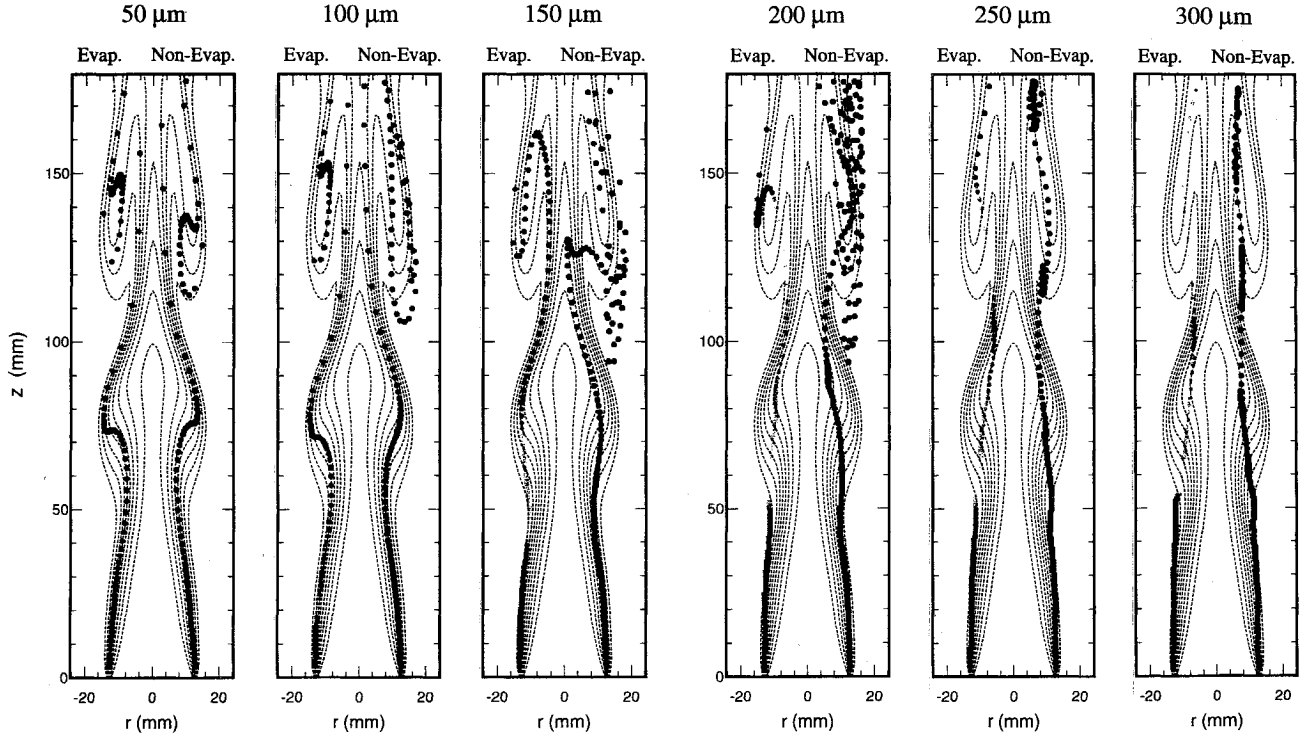

Fig. 10 Simultaneous snapshots of the flow (iso-temperature contours) and droplets (solid circles) of different initial sizes; in each individual snapshot locations of the evaporating and nonevaporating droplets are plotted on the left and right sides of the symmetric jet, respectively.

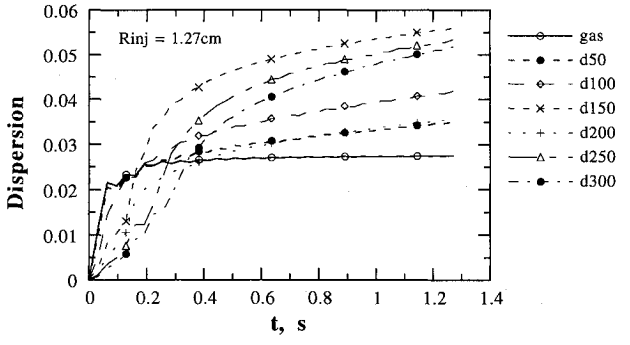

Fig. 11 Variation of dispersion function with time for evaporating droplets at 1*g*.

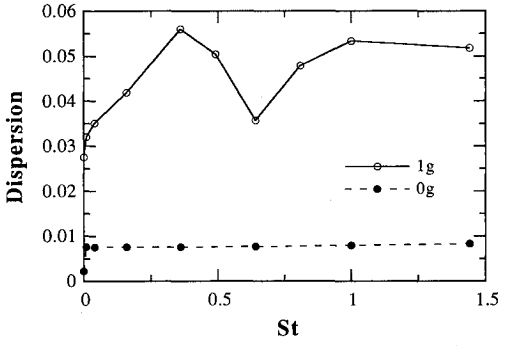

Fig. 12 Variation of dispersion function with Stokes number for the evaporating case at 1 and 0*g*.

be noted from Fig. 10 that in the neighborhood of the second vortex the evaporating droplets are not dispersed as much as the nonevaporating ones are. The reason for this difference may be explained as follows:

The flowfield and the droplet locations near the second vortex are, in fact, the evolution of the respective ones associated with the first vortex. It is known that the entrainment of droplets into the first vortex decreases with the size of the droplet with a maximum occurring for the gas-like particles. On the other hand, as the vortex evolves in space and time, the entrained droplets are centrifuged out of the vortex due to their inertia, which increases with the droplet size. As a result, dispersion of nonevaporating droplets in the neighborhood of the second vortex is more for the medium-sized droplets (~150 μm). However, evaporating droplets exhibit a different behavior. Due to the evaporation process that occurs during the evolution of the flowfield in time and space, the smaller- and medium-sized droplets are not centrifuged out of the second vortex. On the other hand, the larger-sized droplets are not entrained by the first vortex, and hence, are not dispersed in the neighborhood of the second vortex.

Figure 11 shows the variation of dispersion function with time for the gas particle and evaporating droplets for different initial diameter for the 1*g* case. The dispersion function generally increases with time as the droplets, that are continuously being injected into the shear layer, are either pulled radially inward by the heated jet or dispersed radially outward by the large structures. After $t = 0.8$ s, the dispersion function starts leveling out, since some of the injected droplets are being convected out of the computational domain. In order to examine the effect of initial droplet size, it is convenient to plot dispersion function vs size at a fixed t. Figure 12 shows this plot for the 1 and 0*g* cases, where the dispersion function at $t = 1.27$ ms is plotted vs the Stokes number. Three observations can be made from this figure. First, as expected and consistent with the results in Fig. 8, the droplet dispersion for the 0*g* case is negligible compared to that for the 1*g* case. Second, the effect of large vortex structures is to enhance the dispersion of intermediate size droplets. Third, there is a range of Stokes number near $St \sim \mathcal{O}(1)$, where the droplet dispersion behavior is modified by the direct effect of gravity. For example, the maximization of dispersion function for the intermediate Stokes numbers, which is typically observed in the shear-induced vortical structures,[16,17] is modified by gravity. As indicated in Fig. 12, there is a drop in the dispersion

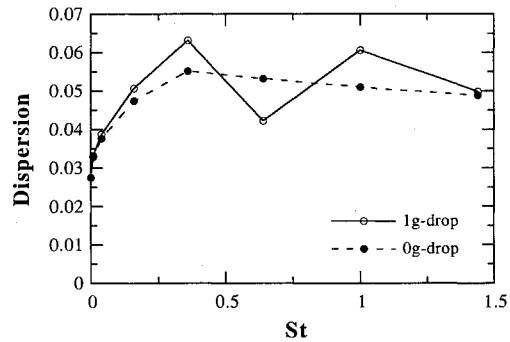

Fig. 13 Variation of dispersion function with Stokes number for nonevaporating droplets with and without the effect of gravity on droplet motion.

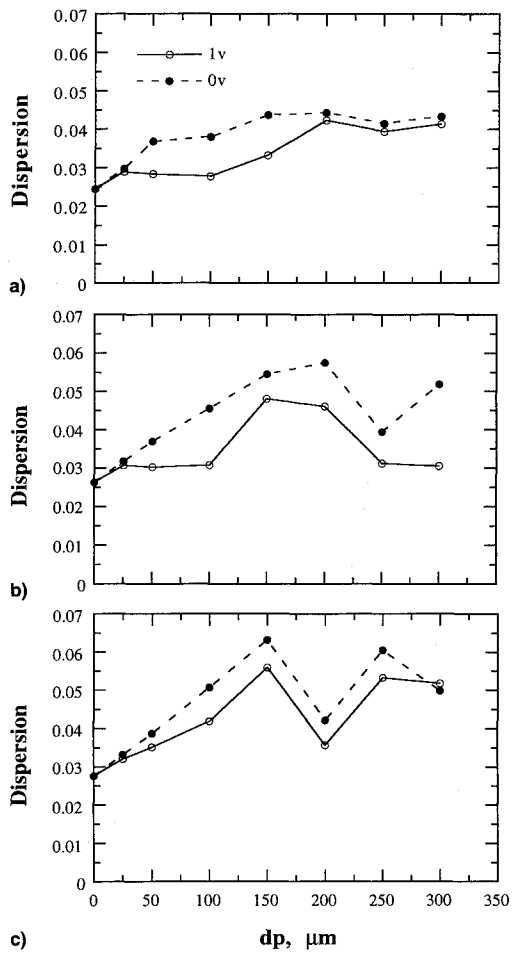

Fig. 14 Variation of dispersion function with initial droplet size for three different injection locations: r_{inj} = a) 1.10, b) 1.20, and c) 1.27 cm. 1*v* and 0*v* represent evaporating and nonevaporating cases, respectively.

function near $St = 0.64$ ($d_p = 200$ μm), which is believed to be due to the fact that the effect of gravity on droplet motion becomes comparable to that of large-scale structures. This is confirmed by performing a dispersion calculation without the effect of gravity on droplet motion. The result given in Fig. 13 for the nonevaporating case indicates that the dispersion function does not experience a drop near $St = 0.64$ ($d_p = 200$ μm), when the gravity term is excluded from the droplet equations. Rather, an optimum droplet size is seen to exist, where the dispersion is maximized. This is consistent with the results of previous experimental[15,16] and computational results.[10,17]

Figure 14 shows the effect of injection location on droplet dispersion for evaporating and nonevaporating droplets at 1*g*. The dispersion function is plotted vs initial droplet size for three injection locations. The important observation is that the maximum droplet dispersion is achieved by injecting droplets in the jet shear layer ($r_{inj} = 1.27$ cm), and that the evaporating droplets are dispersed less compared to the nonevaporating droplets. It is also important to note that as the injection location is moved to the jet core, the dispersion function does not show a sudden drop near $d_p = 200$ μm. This is related to the fact that the direct effect of gravity is not as strong in the jet core region as it is in the shear layer region.

Conclusions

Dynamics and dispersions of *n*-heptane liquid fuel droplets in a heated jet are studied via numerical simulations and flow visualization. The objective of this study is to investigate the droplet dynamics and vaporization behavior in a heated shear layer under normal-gravity and zero-gravity environments. An implicit, third-order accurate upwind numerical scheme is used to solve the unsteady gas-phase equations. The Lagrangian approach is employed to study the droplet dynamics and dispersion in a heated shear layer.

Results show that the gravity has a strong effect on the dynamics of the heated jet shear layer, as well as on the dispersion and vaporization behavior of droplets. The presence of gravity introduces the buoyancy-induced hydrodynamic instability, causing the large vortical structures to appear without any external perturbation. The dynamics of the buoyancy-induced instability in a hot jet is compared to that of the Kelvin-Helmholtz instability in a cold jet. While the large-scale structures in both these cases are highly coherent and periodic with the respective frequencies of 15.8 and 20 Hz, their sizes and convective velocities are significantly different.

The droplets trajectory plots and the simultaneous snapshots of the flow and droplets are employed to analyze the dynamics of nonevaporating and evaporating droplets under the influence of buoyancy-induced vortex structures and gravity. Three different droplet-size regimes are identified to characterize the effects of large structures and gravity. These regimes are distinguished by the values of *St* and *Vr*. In the first regime, characterized by small values of *St* and *Vr*, the droplet behavior is akin to that of gas particles. In the second regime, the droplet dispersion and vaporization behavior is strongly influenced by large vortical structures and gravity, whereas in the third regime, the droplet motion is more strongly affected by the direct effect of gravity.

In order to quantify the effect of gravity and large vortex structures on droplet dynamics, the dispersion function is calculated as a function of initial droplet size for evaporating and nonevaporating droplets for 1 and 0*g* conditions. The important observations are as follows:

1) At zero gravity, in the absence of buoyancy-induced vortex structures, the droplet dispersion is negligibly small compared to that at normal gravity.

2) The effect of large buoyant structures is to enhance the dispersion of intermediate size droplets, and can be represented in terms of the Stokes number.

3) There is a range of Stokes number near unity, where the correlation between dispersion function and Stokes number, reported previously for particle-laden shear flows,[16,17] is modified by the direct effect of gravity.

4) The dispersion behavior of nonevaporating droplets is quite different from that of evaporating droplets. Due to the centrifugal action of the vortical structures, the intermediate-sized nonevaporating droplets disperse more than the gas particles. However, due to the evaporation process, the intermediate-sized evaporating droplets are not centrifuged out of the vortical structures and consequently disperse less than the nonevaporating droplets.

Appendix: Mixture and Fuel Properties

The viscosity and thermal conductivity of the gas mixture are calculated by using the semiempirical formula of Wilke:

$$\mu_m \text{ or } \lambda_m = \sum_{i=1}^{N} \left[X_i(\mu_i \text{ or } \lambda_i) \Big/ \left(\sum_{j=1}^{N} X_j \varphi_{ij} \right) \right]$$

where

$$\varphi_{ij} = \{1 + [(\mu_i \text{ or } \lambda_i)/(\mu_j \text{ or } \lambda_j)]^{1/2}(M_j/M_i)^{1/4}\}^2/(8 + 8M_i/M_j)^{1/2}$$

The mixture specific heat was calculated as a mole fraction weighted average of the specific heats of each contributing species:

$$C_{pm} = \left(\sum_{i=1}^{N} X_i C_{pi} \right) \Big/ M$$

Fuel properties for *n*-heptane were approximated as a function of the temperature from the various sources.[22,23] In this study, the following correlations were used:

latent heat of vaporization

$$L = 316.3(3.204 - T_s/168.6)^{0.38}, \text{ kJ kg}^{-1}$$

vapor mass fraction at the droplet surface

$$Y_{Fs} = \left(1 + \frac{M_g}{M_F} \left\{ \exp \left[\frac{LM_F}{R} \left(\frac{1}{T} - \frac{1}{T_B} \right) \right] - 1 \right\} \right)^{-1}$$

binary diffusion coefficient

$$D = 5.94 \times 10^{-6}(T/273)^{1.60}P^{-1}, \text{ m}^2 \text{ s}^{-1}, \text{ with } P \text{ in atm}$$

vapor specific heat

$$C_{pF} = -51.56 + 6.776T - 3.658 \times 10^{-3}T^2 - 7.673 \times 10^{-7}T^3, \text{ J kg}^{-1} \text{ K}^{-1}$$

vapor thermal conductivity

$$\lambda_F = -4.401 \times 10^{-2} + 2.514 \times 10^{-4}T - 3.173 \times 10^{-7}T^2 + 2.487 \times 10^{-10}T^3, \text{ J m}^{-1} \text{ s}^{-1} \text{ K}^{-1}$$

vapor dynamic viscosity

$$\mu_F = 3.83 \times 10^{-6} - 3.613 \times 10^{-9}T + 4.911 \times 10^{-11}T^2 - 3.577 \times 10^{-14}T^3, \text{ kg m}^{-1} \text{ s}^{-1}$$

Liquid fuel properties were assumed to be constant and evaluated at some average temperature $T_l = (T_0 + T_B)/2 = 332.8$ K. They are as follows:

$$C_{pl} = 2383.89, \text{ J kg}^{-1} \text{ K}^{-1}$$
$$\lambda_l = 1.1768 \times 10^{-1}, \text{ J m}^{-1} \text{ s}^{-1} \text{ K}^{-1}$$
$$\rho_l = 649.38, \text{ kg m}^{-3}$$

Acknowledgments

This work is supported by AFOSR Grant F49620-92-J-0231, with Julian M. Tishkoff as the Program Manager. Many fruitful discussions with W. M. Roquemore at Wright–Patterson Air Force Base, Dayton, Ohio, are greatly appreciated.

References

[1]Ross, H. D., "Overview of NASA's Microgravity Combustion Science and Fire Safety Program," Second International Microgravity Combustion Workshop, Cleveland, OH, 1992.

[2]Burke, S. P., and Schumann, T. E. W., *Industrial and Engineering Chemistry*, Vol. 20, 1928, p. 998.

[3]Hottel, H. C., and Hawthorne, W. R., *Third Symposium on Combustion*, Williams and Wilkins, Baltimore, MD, 1949, p. 254.

[4]Bahadori, M. Y., Edelman, R. B., Stocker, D. P., and Olson, S. L., "Ignition and Behavior of Laminar Gas-Jet Diffusion Flames in Microgravity," *AIAA Journal*, Vol. 28, No. 2, 1990, pp. 236–244.

[5]Bahadori, M. Y., Stocker, D. P., Vaughan, D. F., Zhou, L., and Edelman, R. B., "Effects of Buoyancy on Laminar, Transitional, and Turbulent Gas Jet Diffusion Flames," Second International Microgravity Combustion Workshop, NASA CP 10113, Cleveland, OH, 1992.

[6]Bahadori, M. Y., Hegde, U., Zhou, L., and Stocker, D. P., "Effect of Gravity on the Transition to Turbulence of Gas-Jet Diffusion Flames," AIAA Paper 93-0710, Jan. 1993.

[7]Davis, R. W., Moore, E. F., Roquemore, W. M., Chen, L. D., Vilmpoc, V., and Goss, L. P., *Combustion and Flame*, Vol. 83, 1991, pp. 263–270.

[8]Katta, V. R., and Roquemore, W. M., "Role of Inner and Outer Structures in Transitional Jet Diffusion Flame," *Combustion and Flame*, Vol. 92, 1993, pp. 274–282.

[9]Katta, V. R., Goss, L. P., and Roquemore, W. M., "Effect of Nonunity Lewis Number and Finite-Rate Chemistry on the Dynamics of a Hydrogen-Air Jet Diffusion Flame," *Combustion and Flame*, Vol. 96, 1994, pp. 60–74.

[10]Chung, J. N., and Troutt, T. R., "Simulation of Particle Dispersion in an Axisymmetric Jet," *Journal of Fluid Mechanics*, Vol. 186, 1988, pp. 199–222.

[11]Hansell, D., Kennedy, I. M., and Kollmann, W., "A Simulation of Particle Dispersion in a Turbulent Jet," *International Journal of Multiphase Flow*, Vol. 18, No. 4, 1992, pp. 559–576.

[12]Lazaro, B. J., and Lasheras, J. C., "Particle Dispersion in the Developing Free Shear Layer, Part 1-Unforced Flow," *Journal of Fluid Mechanics*, Vol. 235, 1992, pp. 143–178.

[13]Lazaro, B. J., and Lasheras, J. C., "Particle Dispersion in the Developing Free Shear Layer, Part 2-Forced Flow," *Journal of Fluid Mechanics*, Vol. 235, 1992, pp. 179–221.

[14]Samimy, M., and Lele, S. K., "Motion of Particles with Inertia in a Compressible Free Layer," *Physics of Fluids*, Vol. A3, 1991, pp. 1915–1923.

[15]Hishida, K., Ando, A., and Maeda, M., "Experiments on Particle Dispersion in a Turbulent Mixing Layer," *International Journal of Multiphase Flow*, Vol. 18, No. 2, 1992, pp. 181–194.

[16]Longer, E. K., and Eaton, J. K., "Structure of a Particle-Laden Round Jet," *Journal of Fluid Mechanics*, Vol. 236, 1992, pp. 217–257.

[17]Uthuppan, J., Aggarwal, S. K., Grinstein, F. F., and Kailasanath, K., "Particle Dispersion in a Transitional Axisymmetric Jet: A Numerical Simulation," AIAA Paper 93-0105, Jan. 1993.

[18]Aggarwal, S. K., "Relationship Between Stokes Number and Intrinsic Frequencies in Particle Laden Flows," *AIAA Journal*, Vol. 32, No. 6, 1994, pp. 1322–1325.

[19]Faeth, G. M., "Evaporation and Combustion of Sprays," *Progress in Energy and Combustion Science*, Vol. 9, No. 2, 1983, pp. 1–76.

[20]Aggarwal, S. K., Tong, A., and Sirignano, W. A., "A Comparison of Vaporization Models for Spray Calculation," *AIAA Journal*, Vol. 22, No. 10, 1984, pp. 1448–1457.

[21]Leonard, B. P., "A Stable and Accurate Convective Modelling Procedure Based on Quadratic Upstream Interpolation," *Computational Methods in Applied Mechanics and Engineering*, Vol. 19, 1979, pp. 59–98.

[22]Vargaftik, N. B., *Handbook of Physical Properties of Liquids and Gases*, 2nd ed., Hemisphere, New York, 1983, pp. 632–643.

[23]Ho, C. Y., Liley, P. E., Makita, T., and Tanaka, Y., *Properties of Inorganic and Organic Fluids*, Hemisphere, New York, 1988, pp. 137–150.